

Structure and Stability of Magnetic Fields in Solar Active Region 12192 Based on Nonlinear Force-Free Field Modeling

S. Inoue

*Max-Planck-Institute for Solar System Research, Justus-von-Liebig-Weg 3 37077 Göttingen
Germany*

1

inoue@mps.mpg.de

K. Hayashi

*Institute for Space-Earth Environment Research, Nagoya University, Chikusaku Furo-Cho
Nagoya 464-8601 Japan*

K. Kusano

*Institute for Space-Earth Environment Research, Nagoya University, Chikusaku Furo-Cho
Nagoya 464-8601 Japan*

ABSTRACT

We analyze a three-dimensional (3D) magnetic structure and its stability in large solar active region (AR) 12192, using the 3D coronal magnetic field constructed under a nonlinear force-free field (NLFFF) approximation. In particular, we focus on the magnetic structure that produced an X3.1-class flare which is one of the X-class flares observed in AR 12192. According to our analysis, the AR contains multiple-flux-tube system, *e.g.*, a large flux tube, both of whose footpoints are anchored to the large bipole field, under which other tubes exist close to a polarity inversion line (PIL). These various flux tubes of different

¹Institute for Space-Earth Environment Research, Nagoya University
Furo-cho, Chikusa-ku, Nagoya, 464-8601, Japan

²Japan Agency for Marine-Earth Science and Technology (JAMSTEC), Kanazawa-ku, Yokohama,
Kanagawa, 236-0001, Japan

sizes and shapes coexist there. In particular, the later are embedded along the PIL, which produces a favorable shape for the tether-cutting reconnection and is related to the X-class solar flare. We further found that most of magnetic twists are not released even after the flare, which is consistent with the fact that no observational evidence for major eruptions was found. On the other hand, the upper part of the flux tube is beyond a critical decay index, essential for the excitation of torus instability before the flare, even though no coronal mass ejections (CMEs) were observed. We discuss the stability of the complicated flux tube system and suggest the reason for the existence of the stable flux tube. In addition, we further point out a possibility for tracing the shape of flare ribbons, on the basis of a detailed structural analysis of the NLFFF before a flare.

1. Introduction

The solar storms associated with solar flares, coronal mass ejections (CMEs) strongly affect the electromagnetic environment in our geospace (Kataoka et al. 2014). Therefore, understanding their onset and dynamics is very important not only for obtaining new knowledge of the nonlinear dynamics of the solar coronal plasma but also for establishing space weather forecasting.

Solar active region (AR) 12192, which is the largest AR to date in solar cycle 24 appeared in the middle of October 2014, and is shown in Figure 1(a). Interestingly, this AR produced four X-class flares, (one of which is shown in Figure 1(b)), in just a week, October 20-27, 2014, as shown in Figure 1(c). Nevertheless, CMEs were not observed to accompany these huge flares, whereas Yashiro et al. (2006) reported that flares of such a magnitude are highly likely to be accompanied by CMEs. The ejected flux rope formed via the flare process, which would be central to the occurrence of a CME, is considered to be inhibited by the surroundings, a phenomenon that is well known and often observed as confined flares or eruptions, which have been well studied. For instance, Ji et al. (2003) observed that a filament driven by kink instability was suddenly launched, but it stopped during its ascent, and consequently could not exhibit an eruption. Guo et al. (2010) also reported a good example of confined eruption of a filament on 2005 May 27 in AR 10767, even though the filament showed a strong writhing motion due to highly twisted lines satisfying the condition for the kink instability. More recently, Joshi et al. (2014) analyzed the confined eruption associated with a C-class flare on 2014 January 1 in AR11938. These dynamics showed that two filaments merged by tether-cutting reconnection (Moore et al. 2001), consequently, a long helical filament was formed, and plasma flow was observed as a reconnection jet with

a velocity of more than 200(km/s) along a new long filament. However, no eruptions were seen. Zuccarello et al. (2014) also reported no filament eruptions associated with an M6.0 flare on August 3, 2011 in AR 11261, although a filament eruption occurred later, on August 4.

They reported that the configuration is stable against the torus instability (Kliem & Török 2006). The torus instability is induced by collapse of the force balance between the upward force on a flux tube, *i.e.*, the hoop force driven by a current, and the downward force. The height at which the loop becomes unstable to the torus mode is determined by the decay index in the external field derived from the flux tube’s surroundings. (Török & Kliem 2007, Démoulin & Aulanier 2010), and is specified in the AR of interest, *e.g.*, Guo et al. (2010), Joshi et al. (2014), Zuccarello et al. (2014), Sun et al. (2015). Therefore, stability analysis, in particular, analysis of relationship between the height at which torus instability is excited and the height of the flux tube, is essential for understanding the onset of eruptions. To perform such analysis, we need to determine the magnetic field structures in detail. On the other hand, we cannot directly measure the magnetic field in the solar corona, although extreme ultraviolet (EUV) or X-ray images help us to indirectly determine the flux tube height (*e.g.*, Joshi et al. 2014).

Despite the lack of methods for directly determining the magnetic field in an AR, non-linear force-free field (NLFFF) extrapolation(Wiegelmann & Sakurai 2012) is a robust tool for obtaining information on the three-dimensional(3D) coronal magnetic field. The NLFFF can be extrapolated from three components of the photospheric magnetic field which have been observed by state-of-the-art instruments; the Solar Optical Telescope (SOT:Tsuneta et al. 2008) on board *Hinode* (Kosugi et al. 2007) and the Helioseismic and Magnetic Imager (HMI:Hoeksema et al. 2014) on board *Solar Dynamics Observatory (SDO)*(Scherrer et al. 2012). NLFFF approaches have been used to successfully reconstruct twisted field lines (*e.g.*, Canou et al. 2009, Guo et al. 2010, Jiang et al. 2014, Inoue et al. 2014b, Amari et al. 2014, Inoue et al. 2015), some of these studies analyzed the stability analysis against an ideal magnetohydrodynamic (MHD) instability and tried to explain the onset and dynamics of solar eruptions. Regarding AR12192, Sun et al. (2015) already showed the configuration of the 3D magnetic field but did not address the MHD instability in detail. AR 12192 showed complicated magnetic structure, implying that various flux tubes of different sizes and shapes could coexist there. Therefore, stability analysis should be treated carefully.

In this study, we first extrapolate the 3D magnetic field of AR12192 under the NLFFF approximation(Inoue et al. 2014a), in order to clarify its 3D complex magnetic structure. In particular, we detect the flux tubes making up a knotty magnetic field and discuss the stability. Through these analyses, we eventually answer the question of why no solar eruption

was occurred even though the X3.1-class flare was clearly observed. The rest of this paper is constructed as follows. The observations and numerical method are described in section 2. The results and discussion are presented in sections 3 and section 4, respectively. Our conclusions are presented in section 5.

2. Observation and Numerical Method

2.1. Observation

The vector magnetic fields in the SHARP format (Bobra et al. 2014) are used as the boundary condition of our NLFFF calculation, which is available online ¹. These data are given in a cylindrical equi-area projection. We choose observations at 19:00 UT and 23:00 UT on October 24, approximately 2 h before and after the X3.1-class flare, by HMI/*SDO* (see Figure 2(a)). The data cover a 324×270 (Mm²) region, that is divided into a 900×750 grid and includes a large bipole shaped sunspot in AR12192. They were obtained using the very fast inversion of the Stokes vector algorithm (Borrero et al. 2011) based on the Milne–Eddington approximation. The minimum energy method (Metcalf 1994;Leka et al. 2009) was used to resolve the 180° ambiguity in the azimuth angle of the magnetic field. In this study, the vector field is preprocessed in accordance with Wiegelmann et al. (2006). We also used an EUV image of the coronal magnetic fields taken by the Atmospheric Imaging Assembly (AIA; Lemen et al. 2012) on board *SDO*, for comparison with the NLFFF.

2.2. NLFFF Extrapolation

The NLFFF extrapolation follows the MHD relaxation method developed by Inoue et al. (2014a). The considered equations and parameters are identical as adapted in Inoue et al. (2014b) and Inoue et al. (2015). The basic equations are:

$$\rho = |\mathbf{B}|, \tag{1}$$

$$\frac{\partial \mathbf{v}}{\partial t} = -(\mathbf{v} \cdot \nabla) \mathbf{v} + \frac{1}{\rho} \mathbf{J} \times \mathbf{B} + \nu \nabla^2 \mathbf{v}, \tag{2}$$

¹Data are available at <http://jsoc.stanford.edu/new/HMI/HARPS.html>

$$\frac{\partial \mathbf{B}}{\partial t} = \nabla \times (\mathbf{v} \times \mathbf{B} - \eta \mathbf{J}) - \nabla \phi, \quad (3)$$

$$\mathbf{J} = \nabla \times \mathbf{B}, \quad (4)$$

$$\frac{\partial \phi}{\partial t} + c_h^2 \nabla \cdot \mathbf{B} = -\frac{c_h^2}{c_p^2} \phi, \quad (5)$$

where ρ , \mathbf{B} , \mathbf{v} , \mathbf{J} , ϕ are the pseudo density, magnetic flux density, the velocity, the electric current density, and the convenient potential, respectively. The pseudo density is assumed to be proportional to $|\mathbf{B}|$ in order to make the Alfvén speed relax in space (Amari et al. 1996). The scalar ϕ was introduced by Dedner et al. (2002) to minimize any deviations from $\nabla \cdot \mathbf{B} = 0$. The length, magnetic field, density, velocity, time and electric current density are normalized by $L^* = 324$ Mm, $B^* = 2800$ G, $\rho^* = |\mathbf{B}^*|$, $V_A^* \equiv B^*/(\mu_0 \rho^*)^{1/2}$, where μ_0 is the magnetic permeability, $\tau_A^* \equiv L^*/V_A^*$, and $J^* = B^*/\mu_0 L^*$, respectively. The non-dimensional viscosity ν is set as a constant (1.0×10^{-3}), and the non-dimensional resistivity η is expressed by a functional relation as

$$\eta = \eta_0 + \eta_1 \frac{|\mathbf{J} \times \mathbf{B}| |\mathbf{v}|}{|\mathbf{B}|}, \quad (6)$$

where $\eta_0 = 5.0 \times 10^{-5}$ and $\eta_1 = 1.0 \times 10^{-3}$ in the non-dimensional unit. The second term is introduced to accelerate the relaxation to the force-free field, particularly in the weak field region. The other parameters c_h^2 and c_p^2 are fixed to constants 0.04 and 0.1, respectively. The velocity is controlled as follows. If the value of v^* becomes larger than v_{max} (here set to 0.01), then the velocity is modified as follows: $\mathbf{v} \Rightarrow (v_{max}/v^*)\mathbf{v}$. This process can suppress large discontinuities produced between the bottom and inner domain.

The potential field is given as the initial condition, which is extrapolated only from the normal component of the photospheric magnetic field. During the iteration, three components of the magnetic field are fixed at each boundary while the velocity is fixed to zero and the von Neumann condition $\partial/\partial n=0$ is imposed on ϕ . Note that the bottom boundary is fixed according to

$$\mathbf{B}_{bc} = \zeta \mathbf{B}_{obs} + (1 - \zeta) \mathbf{B}_{pot},$$

where \mathbf{B}_{bc} is the horizontal component which is determined by a linear combination of the observed magnetic field (\mathbf{B}_{obs}) and the potential magnetic field (\mathbf{B}_{pot}). ζ is a coefficient ranging from 0 to 1. When $R = \int |\mathbf{J} \times \mathbf{B}|^2 dV$, which is calculated over the interior of the computational domain, falls below a critical value denoted by R_{min} during the iteration, the value of the parameter ζ is increased to $\zeta = \zeta + d\zeta$. In this paper, R_{min} and $d\zeta$ have the

values 5.0×10^{-3} and 0.02, respectively. If ζ becomes equal to 1, \mathbf{B}_{bc} is completely consistent with the observed data. This process also helps to avoid a sudden jump from the boundary into the domain. A numerical box with dimensions of $324 \times 270 \times 270$ (Mm^3) is given as $1 \times 0.8333 \times 0.8333$ in its non-dimensional value. A 3×3 binning of the original data yields a grid resolution of $300 \times 250 \times 250$.

3. Results

3.1. Overview of 3D Magnetic Structure Before the X3.1-Class Flare

Figure 2(a) shows the photospheric magnetic field obtained from *SDO*/HMI at 19:00 UT on October 24 2014, which is approximately 2h before the X3.1-class flare; the NLFFF calculation was applied to this field as the bottom boundary condition. We can see large negative and positive sunspots in the center of the field, whereas a region close to the PIL between them is filled with complex magnetic structure of mixed positive and negative polarities. Figure 2(b) shows the 3D structure of the magnetic field lines of the NLFFF based on the photospheric magnetic field shown in Figure 2(a). We found the sheared field lines between the major sunspots, whereas the area outside of them is filled with the closed field lines in a potential field like structure. Figure 2(c) shows an EUV image obtained from *SDO*/AIA 94 Å, whose covers a region identical in size to that in Figure 1(a). The field lines of the NLFFF are superimposed on the EUV image in Figure 2(d); the color indicates the strength of the current density $|\mathbf{J}| = \sqrt{j_x^2 + j_y^2 + j_z^2}$. Field lines having strong current density are obviously concentrated in the central region, in which the EUV is also strongly enhanced, as shown in Figure 2(c)

3.2. Magnetic Twist of the NLFFF Before the X3.1 Class Flare

To understand the physical aspects of the NLFFF, we have to detect the essential feature in the complicated magnetic field in Figure 2(b). In particular, because a flux tube, which is a bundle of highly twisted lines, is a major candidate for the driver of solar eruptions, it plays an important role in eruption onset and we need to correctly understand its stability. First, to locate the flux tube, we calculate the magnetic twist, which is defined as follows:

$$T_n = \frac{1}{4\pi} \int \frac{\mathbf{J}_{\parallel}}{|\mathbf{B}|} dl, \quad (7)$$

where $\mathbf{J}_{\parallel}(= \mathbf{J} \cdot \mathbf{B}/|\mathbf{B}|)$ is the field-aligned current. The magnetic twist is a turn of the field lines corresponding to the magnetic helicity generated by the field-aligned current (Berger &

Prior 2006), and has been applied to several ARs (*e.g.*, Inoue et al. 2011; Inoue et al. 2012; Inoue et al. 2013).

Figure 3(a) shows the contour of the half-turn twist obtained from the NLFFF, mapped on the B_z distribution approximately 2h before the X3.1-class flare. Note that this twist is left-handed; therefore, its value of twist is $T_n = -0.5$. The interior regions surrounded by the contours are occupied by twisted lines with more than half-turn twist (“strongly twisted lines” hereafter); *i.e.*, these regions are occupied by the footpoint of the flux tube. According to this figure, the strongly twisted lines dominate in a wide region close to and distant from the PIL. The former is along the PIL, whereas the later exits on the magnetic flux constituting the major bipole field of the AR. Figure 3(b) shows the 3D structure of the magnetic field lines traced from the regions inside of the contours. We found flux tubes of different sizes and shapes; here, these are roughly separated into two components. The first component is anchored in the major bipole fields, and the second component is a small flux tube underneath the first. Figure 3(c) depicts the same field lines from the top with the strength of the current density $|\mathbf{J}|$ superimposed. According to this figure, the twisted lines close to the solar surface have a strong current density, unlike that accumulated in the large flux tube above them. Figure 3(d) shows the twist distribution versus $|B_z|$. We found that most of the field lines are less than one turn, which implies that the magnetic field was stable against kink mode instability before the X3.1-class flare. Therefore kink instability can be eliminated as a candidate for the driver of the flare.

3.3. Magnetic Twist of the NLFFF After the X3.1 Class Flare

Figure 4 shows the same plot as in Figure 3, but for the second instant (23:00 UT) which is approximately 2h after the flare. These profiles are quite similar to those obtained before the flare, indicating that the current density and magnetic twist accumulated before the flare seem to be conserved overall (see Figures 4(c) and (d)) despite the occurrence of the X-class flare. This tendency is quite different from that found for other ARs, *e.g.*, AR10930 (Inoue et al. 2012) or AR11158 (Inoue et al. 2013). Those studies reported that most of the strongly twisted lines with more than half-turn twist disappear after X-class flares, and some of them are converted into post-flare loops. This is a result of the process in which the magnetic twists accumulated in the ARs are expelled to the upper corona. However, the results obtained from this study are consistent with the fact that CMEs were not observed in via several X-class flares.

3.4. Twisted Lines Producing the X3.1-class Flare

In this section, we confirm which twisted lines produced the X3.1-class flare. To do so, we compare the field lines of the NLFFF before the flare with the two-ribbon flares obtained from Ca II image taken from a filtergram of *Hinode*. Figure 5(a) shows the two-ribbon flares observed in the early phase of the flare taken by *Hinode* together with the contours of half-turn twist obtained from the NLFFF before the flare. In Figure 5(b) we further plot selected field lines, both of the footpoints of which are anchored in the enhanced region of Ca II. We found that these are sheared field lines, and a strong current is carried there. In the tether-cutting model, sheared two-ribbon flares appear initially in regions corresponding to the footpoints of sheared field lines in the onset phase owing to reconnection between them. According to this scenario, these field lines close to the solar surface would be related to the X3.1-class flare.

We add other twisted lines in Figure 5(c) and show a side view in Figure 5(d); these lines are larger than the twisted lines shown in Figure 5(b) and straddle them. The twisted lines making up the large flux tube are traced from region A, marked in Figure 5(a), and surrounded by a half turn twist contour, but strong enhancement of Ca II was not observed during the flare. These field lines also consist of strongly twisted lines with more than half-turn twist, but they are not related to the X3.1-class flare. If these field lines are quite stable, they might suppress the eruption accompanying with the flare. We later discuss the stability of these twisted lines.

3.5. Location that Two-Ribbon Flares are Enhanced.

In the previous section, we found that in the first instant the twisted lines were anchored in the flare-ribbon region, which might be a signature of magnetic reconnection. On the other hand, all of the twisted lines are unrelated to the X3.1-class flare; rather, the two-ribbon flare seemed to run close to the edge of the region where the strongly twisted lines reside (see Figure 5(a)).

Reconnection is considered to occur relatively easily in the separatrix layer (Longcope 2005; Démoulin 2006; Titov et al. 2009) because it is a boundary between regions of magnetic field lines with different connectivity, and formation of a thin current layer would be favorable there. However, the observed two-ribbon flares appear in a limited area; *i.e.*, they do not cover all of the separatrix on the solar surface. We clarify the structure of the two-ribbon flare in comparison with the magnetic field by exploring the location of the quasi-separatrix layer (QSL) on the solar surface and the twist derived from the NLFFF.

We calculate the norm of the Jacobi matrix for magnetic field, following Demoulin et al. (1996):

$$N(x, y) = \text{sgn}(B_z) \sqrt{\sum_{i=1,2} \left[\left(\frac{\partial X_i}{\partial x} \right)^2 + \left(\frac{\partial X_i}{\partial y} \right)^2 \right]}, \quad (8)$$

where (X_1, X_2) is the end point of a field line traced from the other footpoint at position (x, y) and $\text{sgn}(B_z)$ is defined by

$$\text{sgn}(B_z) = \begin{cases} -1 & B_z < 0, \\ 1 & B_z > 0. \end{cases}$$

The differentials in the x and y directions are approximated by the grid interval. This means that the locations of the end points of two field lines that are traced from these starting points across a large $N(x, y)$ value may differ greatly.

Figures 6(a) and (b) show the B_z distribution with the PIL observed at 19:00 UT (before the flare) and a map of $N(x, y)$ (or more precisely, of its logarithm) obtained from the NLFFF, respectively, both of which are plotted in the same area. The connectivity of the field lines changes dramatically across the regions where the $N(x, y)$ is large; consequently, some of the QSLs would easily produce the current layer, and reconnection might occur more easily there than in other areas. On the other hand, because not all of the QSLs on the solar surface is connected with solar flares, we need to extract the proper areas related to them from the map of $N(x, y)$.

The magnetic twist is also an important proxy as well as N in considering the onset of solar eruptions, and it might help us to specify the QSL at which the flare is strongly connected. Figure 6(c) shows the twist distribution of more than half-turn twist before the flare superimposed on Figure 6(b). We found that the boundaries of the twist can partially overlap with those of the strong enhancement layers of $N(x, y)$, and these regions appear to be similar in shape to the flare ribbons shown in Figure 5(a). To confirm this, we further calculate $|T_n \times N|$ in a range of $T_n \leq -0.5$ and $|N| \geq 1$, and plotted it in Figure 6(d) with the flare ribbons. The contours of $|T_n \times N|$ roughly capture the distribution of the flare ribbons. Furthermore, in Figure 6(e), we plot the $|T_n \times N|$ with another contour level having a higher value than that shown in Figure 6(d). We found that most of the contours are along the edge of the ribbons; *i.e.*, the strongly enhanced layer of N would correspond to the boundary of the flare ribbons. This interpretation is consistent with a growth of the flare ribbons being inhibited by the QSL, as suggested by Chen et al. (2011). These results suggest that the flare ribbons are not related to just the intersection of the QSL with the solar surface or the twistedness, but that both pieces of information are needed. From another view point, interestingly, the shape of the flare ribbons might be predicted from the NLFFF before a flare.

4. Discussion

4.1. Stability Against the Torus Instability

In the previous section, we first saw that the NLFFF reconstructed 2h before the X3.1-class flares is stable to kink mode instability. We further discuss the stability against torus instability as well. The torus instability is caused by a process, in which the force balance acting on the flux tube is broken, where the upward force is the hoop force due to a current in the flux tube and the downward force is contributed by the surroundings. A criterion where the instability can occur is defined by the decay index (Kliem & Török 2006),

$$n = -\frac{z}{|\mathbf{B}|} \frac{\partial |\mathbf{B}|}{\partial z}, \quad (9)$$

which is calculated from the external field surrounding the flux tube. Several earlier studies noted that instability happens at the condition $n=1.5$ (*e.g.*, Török & Kliem 2007).

Figure 7(a) shows the twisted field lines with more than a half-turn twist at 19:00 UT, *i.e.*, approximately 2h before the X3.1-class flare, where the colors represent the different values of n . We clearly found that the upper half of TL1 indicated in Figure 7(a) satisfies $n \geq 1.5$, even though most of TL2 meets $n \leq 1.0$. Figure 7(b) shows the height profile of the decay index where this decay index is averaged in the $x - y$ plane

$$\langle n(z) \rangle = \frac{1}{N_x N_y} \sum_{i,j}^{N_x, N_y} n(x_i, y_j, z), \quad (10)$$

where N_x and N_y are grid number in the calculated area in the x and y directions, respectively. According to these results, $n=1.5$ corresponds to approximately 70-80(Mm). This result is consistent with Sun et al. (2015), which further reported that this height is greater than that estimated in other ARs (*e.g.*, AR11158, AR11429). From our results, we found that most of the twisted lines connected with the X-class flares, *i.e.*, TL2 in Figure 7(a), reside in an area that is stable against the torus instability. On the other hand, the top part of TL1 exceeds even $n=2.0$ in its twistness. The twisted lines obviously meet the unstable condition; nevertheless, CMEs associated with the huge flare were not observed from this AR.

The major reason for the suppressing of the instability of the upper flux tube, TL1, is that the electric current flowing in the flux tube is not well approximated by a single line current loop, which was used in the theory of torus instability (Kliem & Török 2006). The decay index is derived from the external field, in which the flux tube approximated by the loop of a single current line stays in an equilibrium state, but there is no guarantee that this

scenario applies in this magnetic field in which the current is widely distributed as shown in Figure 8(a), where the current is divided by $|\mathbf{B}|$ at each place. Figure 8(b) shows the field lines colored according to $|\mathbf{J}|/|\mathbf{B}|$. The vertical extended current produces a long vertical flux tube, which deviates greatly from the flux tube derived from a single loop current. From another viewpoint, because variable magnetic flux tubes of different size and shapes cross the vertically extended electric current distribution, the stability of these complex magnetic structure may not be easily determined. For instance, we consider a simple situation in which a double-decker flux tube (Liu et al. 2012; Cheng et al. 2014) is assumed and each flux tube has a line current in the same direction. Then the downward force, *i.e.*, the pinch force, due to the current in the lower twisted lines acts on the upper twisted lines. Obviously this pinch force causes the upper twisted lines to enter a stable condition. In other words, because the hoop force on the upper flux tube is weakened, we can suggest that the height of the typical loop taken up in the instability would decrease. Nevertheless, the hoop force works efficiently on the lower twisted lines (TL2), but these are mostly stable; *i.e.*, this mechanical interaction between the different twisted flux ropes (TL1 and TL2) might keep the stability.

4.2. MHD Simulation to Confirm the Stability

In this paper, we discussed the stability of the NLFFF, using the magnetic twist as expressed in Equation (7) together with decay index as defined by Equation (9). However, this analysis is not rigorous because these criteria were derived under certain assumptions and there is no guarantee these assumptions are also valid for our NLFFF model. Therefore, in order to obtain further confirmation of the stability of the configuration, we performed an MHD simulation using the NLFFF at 21:00 UT as the initial condition, and neglecting external forces. On the other hand, since the NLFFF is calculated numerically, it is not completely in force balance and hence a residual force exists, which plays the role of a perturbation. Therefore if the NLFFF would be unstable, the unstable mode should grow exponentially, resulting in an increase of the kinetic energy and a deformation of the magnetic structure.

The MHD simulation is identical to that performed in Inoue et al. (2014b) and Inoue et al. (2015), whose Equations (1)-(5) are being solved but here a constant resistivity $\eta=5.0\times 10^5$ is chosen. The velocity is controlled only on the nearby side boundaries according to the manner described in Section 2.2, so that the numerical noise could be suppressed. Regarding to the boundary condition, the normal component of the magnetic field B_n is fixed on all boundaries, and the horizontal components \mathbf{B}_t are determined by the induction equation.

The velocity field is fixed to zero and the same von Neumann boundary condition as in the NLFFF calculation is imposed on ϕ .

Figure 9(a) shows the temporal evolution of the kinetic energy ($E_k = \int \rho |\mathbf{v}^2|/2 \, dV$). Although the value once increases suddenly around $t=1.0$, the growth stops there after and quickly decreases when $t > 1.0$. This sudden increase is excited by the residual velocity which cannot be removed from the NLFFF. Figure 9(b) exhibits the temporal evolution of the 3D magnetic structures. The drawn magnetic field lines exhibit little changes in structures over a long span of time, as seen at $t=2.0$, $t=6.0$ and $t=10.0$. We found that the vertical velocity on the twisted lines is also getting small in the temporal evolution. Finally, we also confirm the facts that whether or not the boundary condition prevents the growth of the instability. Figure 9(c) shows the temporal evolution of the vertical profile on $|\mathbf{B}|^2$ where $|\mathbf{B}|^2 = B_x^2 + B_y^2 + B_z^2$. We can find an imperceptible variation around the top boundary, *i.e.*, no enhancement in the vicinity of the top boundary would give no feedback to the flux tube. Therefore, these results also support that the NLFFF is stable against the MHD instability.

5. Summary

This paper presents the structure and stability analysis of the 3D magnetic fields of large solar AR 12192 reconstructed under the NLFFF approximation before and after the X3.1-class flare that occurred around 21:00 UT on October 24 2014. This AR contains two huge major bipoles and also a complex magnetic structure of mixed positive and negative polarities close to the PIL. The 3D configuration of the magnetic field is also not so simple. We found a multiple-flux-tube system composed of variable twisted lines of different shapes and sizes. This includes a large flux tube anchored to the main polarities, under which several flux tubes exist along the PIL. In particular, the later configuration(lower one) is favorable for the tether-cutting reconnection, and the location of their footpoints corresponds to the area in which two-ribbon flares are strongly enhanced during the X3.1-class flare. This means that the upper twisted lines are not related to that flare.

The stability of the magnetic configuration was also analyzed. We estimated the magnetic twist to confirm the stability against the kink instability; since the most of the twisted lines have a twist less than one turn, we, therefore, conclude that the NLFFF is in stable state against kink instability. On the other hand, some of the upper twisted lines are in the region of over the critical decay index for the torus instability, even though an eruption was not observed from this AR in the middle of October 2014. Hence we suggest that this estimation of the critical decay index cannot be applied to the multiple-flux-tube system. The existing theory was established where current was confined to a single loop current inside

the flux tube, but in practice the current is distributed in the solar corona. For the present study, because we have to consider the interaction of each flux tube, it would not be easy to estimate the loop height at which the instability is excited. Although all of these stability analyses are performed based on the linear stability analysis, we further numerically confirm the stability through MHD simulation.

Finally we discussed the location at which the two ribbon flares appear. On the basis of our results, we suggested that the location at which flare ribbons appear might be specified using both QSL defined by large N and a strong magnetic twist, in particular, a region in which strong enhancement of N corresponds to the boundaries of the flare ribbons. This simply means that the discontinuity region composed of strongly twisted lines, especially those with more than half-turn twist, would be a candidate for producing huge solar flares. With future development, we expect that this concept may be a useful method for predicting solar flares which in turn may lead to the space weather prediction.

We are grateful to referee for his/her constructive comments and Dr. Vinay Shanker Pandey for reading the proof version of this paper. This work was supported by JSPS KAKENHI Grant Numbers 23340045, and 15H05814. S. I. sincerely thanks to the Alexander von Humboldt foundation for supporting his stay in Germany as well as this work. The computational work was carried out within the computational joint research program at the Solar-Terrestrial Environment Laboratory, Nagoya University. Computer simulation was performed on the Fujitsu PRIMERGY CX400 system of the Information Technology Center, Nagoya University. The computational resources for the data analysis and visualization system by using resource of the OneSpaceNet in the NICT Science Cloud and VAPOR (Clyne & Rast 2005, Clyne et al. 2007).

REFERENCES

- Amari, T., Luciani, J. F., Aly, J. J., & Tagger, M. 1996, *ApJ*, 466, L39
- Amari, T., Canou, A., & Aly, J.-J. 2014, *Nature*, 514, 465
- Berger, M. A., & Prior, C. 2006, *Journal of Physics A Mathematical General*, 39, 8321
- Bobra, M. G., Sun, X., Hoeksema, J. T., et al. 2014, *Sol. Phys.*, 289, 3549
- Borrero, J. M., Tomczyk, S., Kubo, M., et al. 2011, *Sol. Phys.*, 273, 267
- Canou, A., Amari, T., Bommier, V., et al. 2009, *ApJ*, 693, L27

- Chen, P. F., Su, J. T., Guo, Y., & Deng, Y. Y. 2011, arXiv:1109.0381
- Cheng, X., Ding, M. D., Zhang, J., et al. 2014, ApJ, 789, 93
- Clyne, J., & Rast, M. 2005, Proc. SPIE, 5669, 284
- Clyne, J., Mininni, P., Norton, A., & Rast, M. 2007, New Journal of Physics, 9, 301
- Dedner, A., Kemm, F., Kröner, D., et al. 2002, Journal of Computational Physics, 175, 645
- Démoulin, P., & Aulanier, G. 2010, ApJ, 718, 1388
- Demoulin, P., Henoux, J. C., Priest, E. R., & Mandrini, C. H. 1996, A&A, 308, 643
- Démoulin, P. 2006, Advances in Space Research, 37, 1269
- Guo, Y., Ding, M. D., Schmieder, B., et al. 2010, ApJ, 725, L38
- Hoeksema, J. T., Liu, Y., Hayashi, K., et al. 2014, Sol. Phys., 289, 3483
- Inoue, S., Magara, T., Pandey, V. S., et al. 2014a, ApJ, 780, 101
- Inoue, S., Hayashi, K., Magara, T., Choe, G. S., & Park, Y. D. 2014b, ApJ, 788, 182
- Inoue, S., Hayashi, K., Magara, T., Choe, G. S., & Park, Y. D. 2015, ApJ, 788, 182
- Inoue, S., Kusano, K., Magara, T., Shiota, D., & Yamamoto, T. T. 2011, ApJ, 738, 161
- Inoue, S., Shiota, D., Yamamoto, T. T., et al. 2012, ApJ, 760, 17
- Inoue, S., Hayashi, K., Shiota, D., Magara, T., & Choe, G. S. 2013, ApJ, 770, 79
- Ji, H., Wang, H., Schmahl, E. J., Moon, Y.-J., & Jiang, Y. 2003, ApJ, 595, L135
- Jiang, C., Wu, S. T., Feng, X., & Hu, Q. 2014, ApJ, 780, 55
- Joshi, N. C., Magara, T., & Inoue, S. 2014, ApJ, 795, 4
- Kataoka, R., Sato, T., Kubo, Y., et al. 2014, Space Weather, 12, 380
- Kliem, B., Török, T. 2006, Physical Review Letters, 96, 255002
- Kosugi, T., Matsuzaki, K., Sakao, T., et al. 2007, Sol. Phys., 243, 3
- Leka, K. D., Barnes, G., Crouch, A. D., et al. 2009, Sol. Phys., 260, 83
- Lemen, J. R., Title, A. M., Akin, D. J., et al. 2012, Sol. Phys., 275, 17

- Liu, R., Kliem, B., Török, T., et al. 2012, *ApJ*, 756, 59
- Longcope, D. W. 2005, *Living Reviews in Solar Physics*, 2, 7
- Metcalf, T. R. 1994, *Sol. Phys.*, 155, 235
- Moore, R. L., Sterling, A. C., Hudson, H. S., & Lemen, J. R. 2001, *ApJ*, 552, 833
- Savcheva, A., Pariat, E., McKillop, S., et al. 2015, arXiv:1506.03452
- Scherrer, P. H., Schou, J., Bush, R. I., et al. 2012, *Sol. Phys.*, 275, 207
- Sun, X., Bobra, M. G., Hoeksema, J. T., et al. 2015, *ApJ*, 804, L28
- Titov, V. S., Forbes, T. G., Priest, E. R., Mikić, Z., & Linker, J. A. 2009, *ApJ*, 693, 1029
- Török, T., & Kliem, B. 2007, *Astronomische Nachrichten*, 328, 743
- Tsuneta, S., Ichimoto, K., Katsukawa, Y., et al. 2008, *Sol. Phys.*, 249, 167
- Wiegmann, T., & Sakurai, T. 2012, *Living Reviews in Solar Physics*, 9, 5
- Wiegmann, T., Inhester, B., & Sakurai, T. 2006, *Sol. Phys.*, 233, 215
- Yashiro, S., Akiyama, S., Gopalswamy, N., & Howard, R. A. 2006, *ApJ*, 650, L143
- Zuccarello, F. P., Seaton, D. B., Mierla, M., et al. 2014, *ApJ*, 785, 88

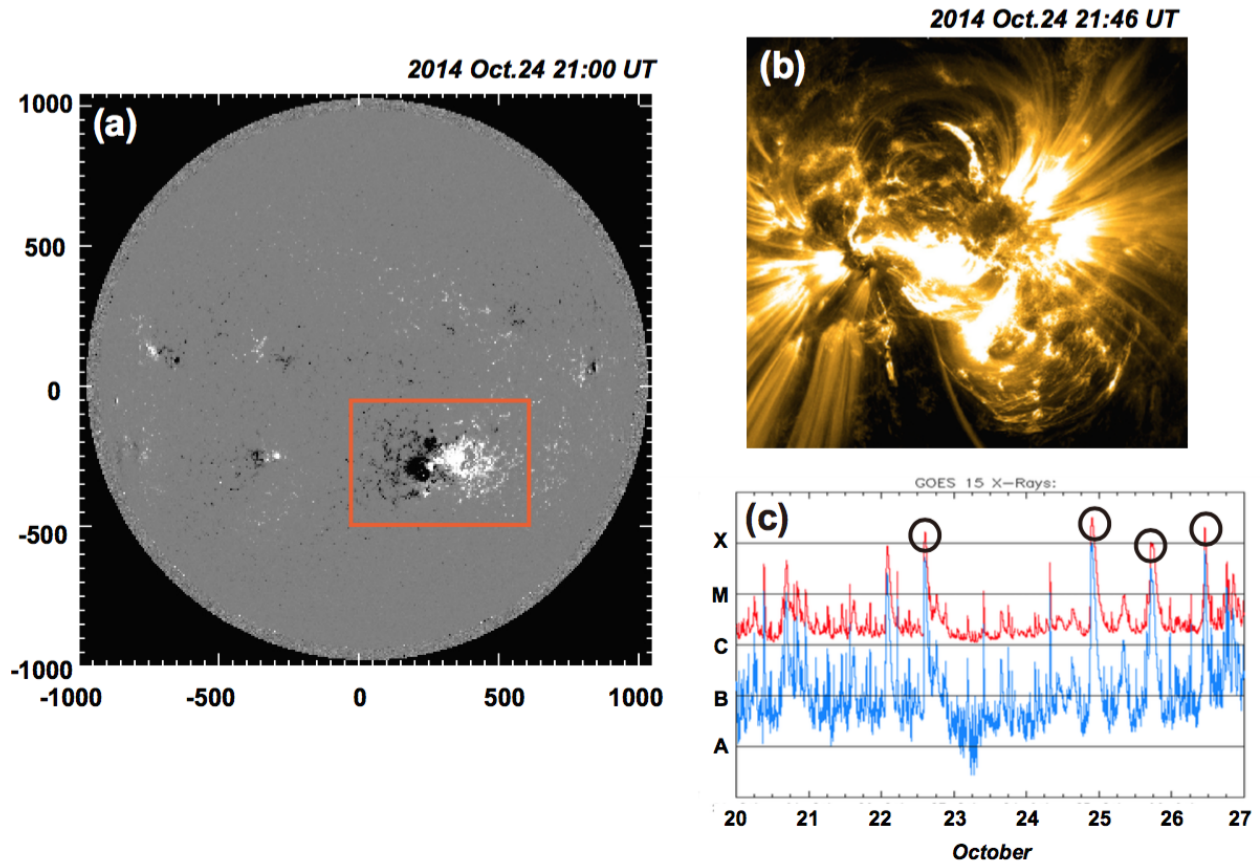


Fig. 1.— (a) Full-disk image of a line-of-sight component of the solar magnetic field observed at 21:00 UT on October 24 in an onset phase of an X3.1-class flare by *SDO*/HMI. (b) EUV image during the X3.1-class flare observed at 21:46 UT by *SDO*/AIA 171 Å. (c) Time profile of the X-ray flux measured by the GOES 12 satellite from October 20 to 27, 2014. The solar X-ray outputs in the 1–8 Å and 0.5–4.0 Å passband are plotted, respectively. Four X-class flares were observed during this period.

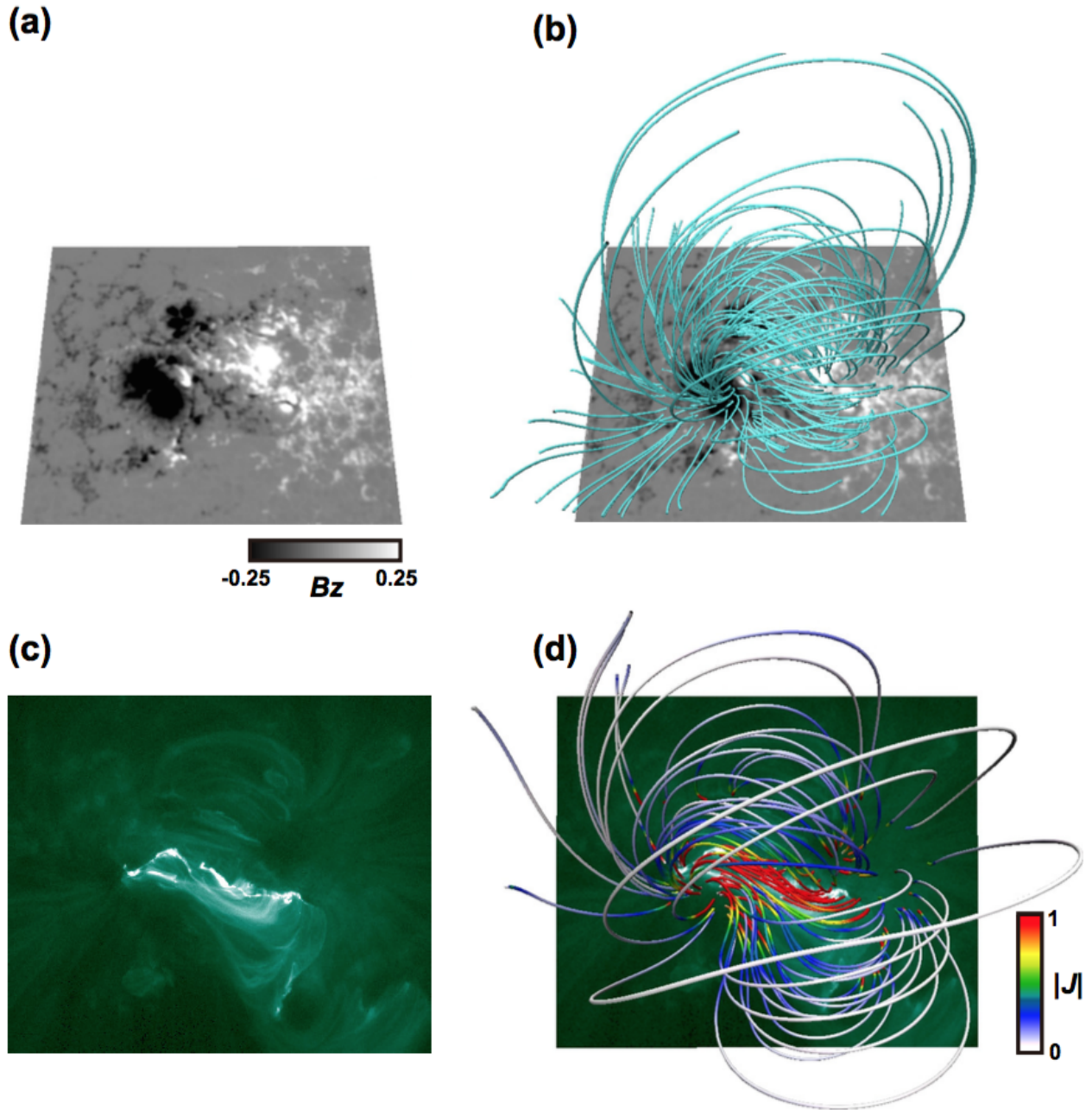


Fig. 2.— (a) Normal component B_z of the photospheric magnetic field observed at 19:00 UT on October 24, which is approximately 2h before the X3.1-class flare. (b) Filed lines of the NLFFF are plotted over (a). (c) The EUV image observed at 21:10:50 UT on October 24 2014 by *SDO/AIA*. (d) Field lines are plotted over (c). Color indicates the strength of the current density ($|\mathbf{J}|$).

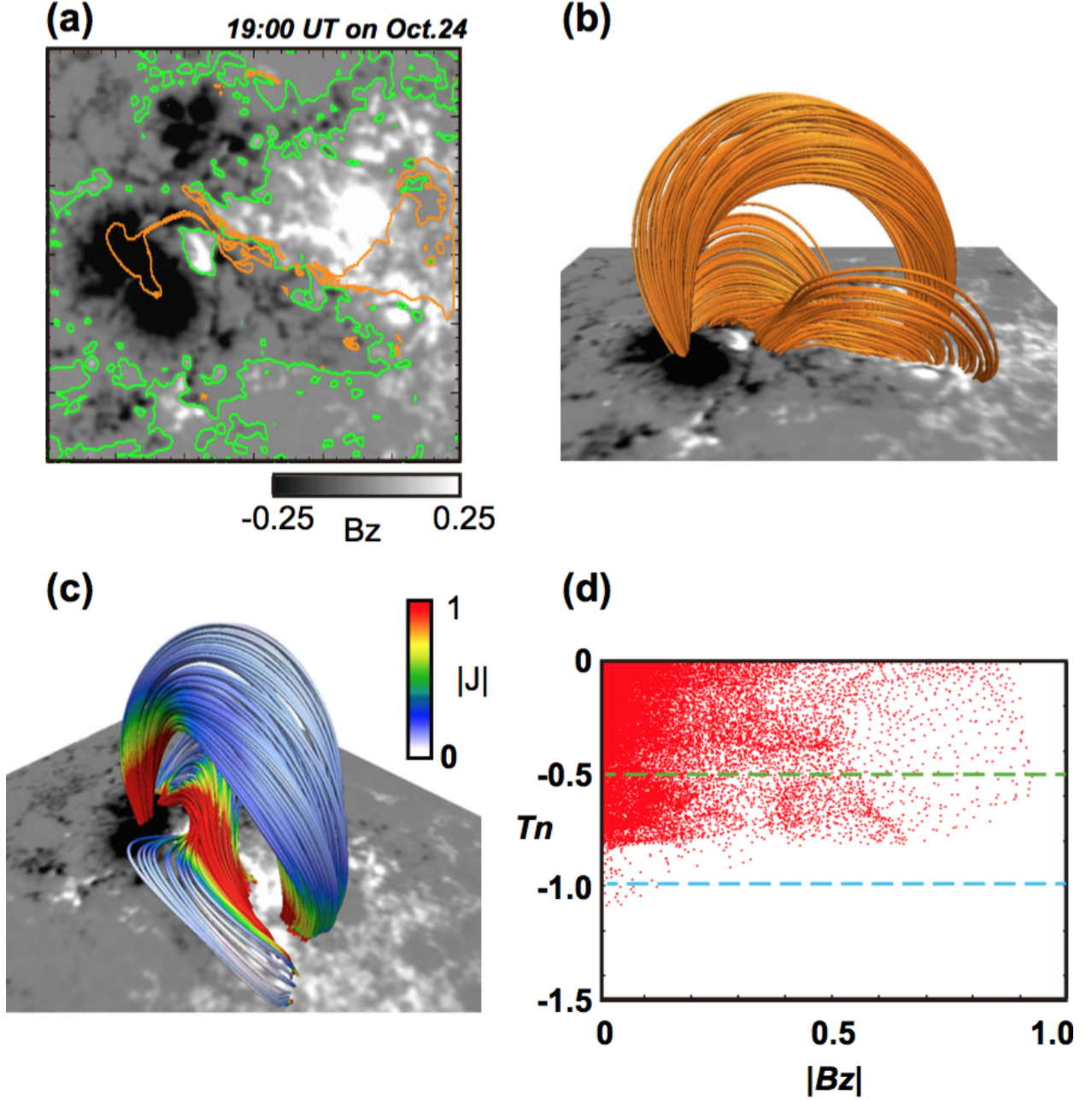


Fig. 3.— (a) Normal component B_z of the magnetic fields taken approximately 2h before the X3.1 class flare (19:00 UT), together with contour of the half-turn twist (left-handed twist) calculated from the NLFFF (orange lines) and PIL (green lines). The calculation is performed in the range of $0.2L_0 \leq x \leq 0.8L_0$ and $0.1L_0 \leq y \leq 0.7L_0$. (b) Three-dimensional structure of the field lines of the NLFFF (orange), with B_z distribution. All of the field lines are twisted with more than a half-turn. (c) Same field lines as in (b) except that the color depends on the strength of the current density $|J|$. (d) Twist distribution versus $|B_z|$. Blue and green dashed lines indicate one-turn and half-turn twist, respectively.

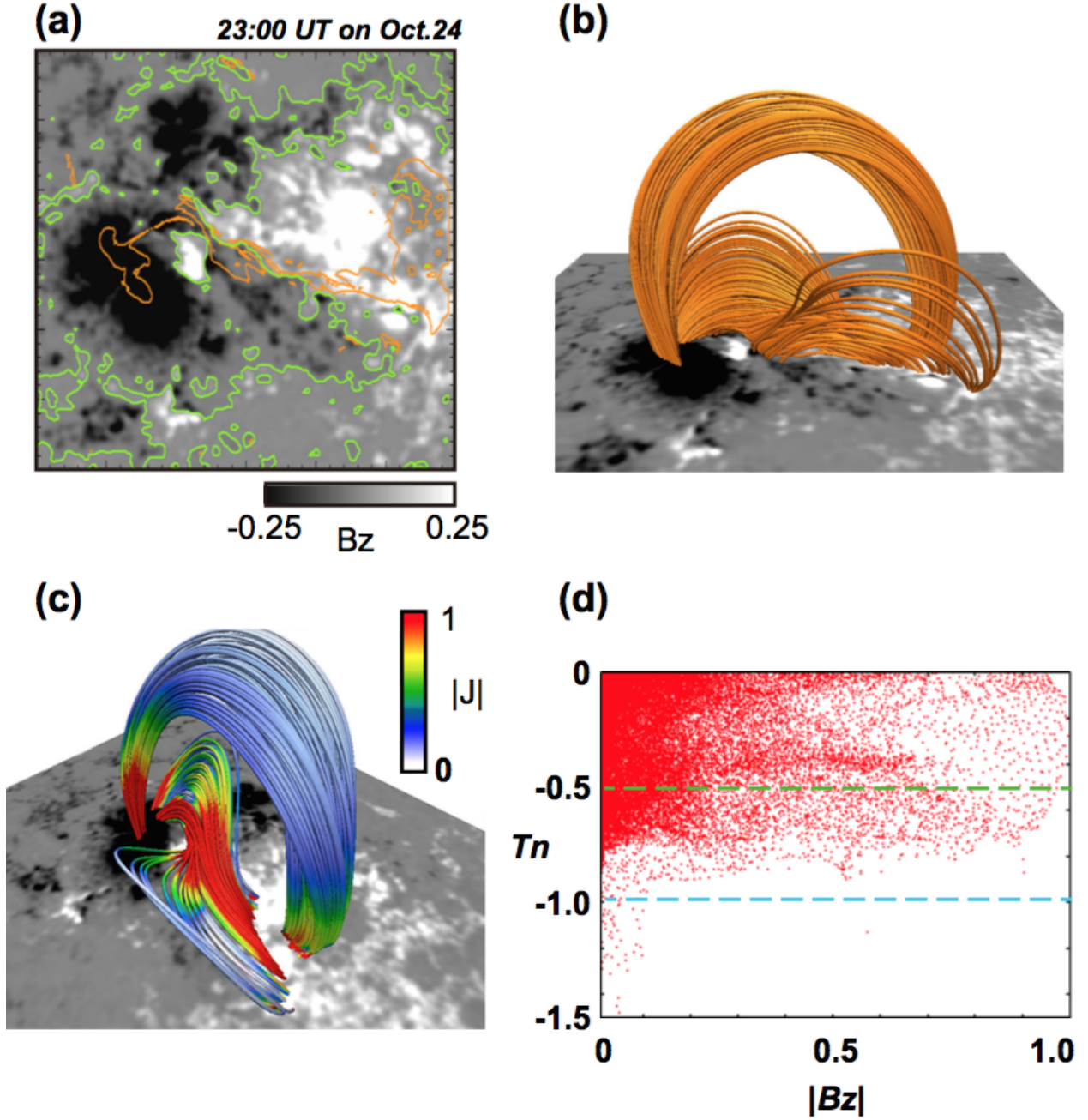


Fig. 4.— (a) Normal component B_z of the magnetic fields taken at 23:00 UT on October 24, which is approximately 2h after the X3.1-class flare, together with contours of the half-turn twist calculated from the NLFFF and PIL. The format is the same as that of Figure 3(a). (b) Field lines of the NLFFF with more than half-turn twist and the B_z distribution; the format is the same as that of Figure 3(b). (c) $|J|$ is mapped on the field lines depicted in (b). (d) Twist distribution versus $|B_z|$. The format is the same as that of Figure 3(d).

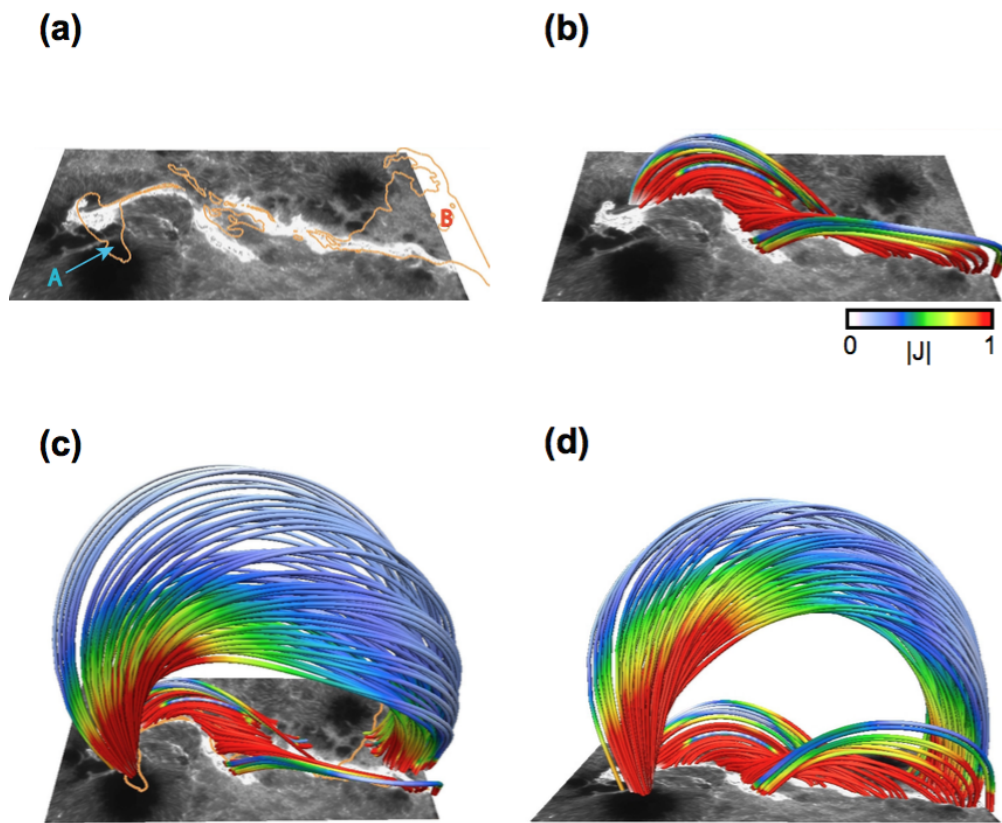


Fig. 5.— (a) Two-ribbon flares of X3.1-class flare observed in early phase of the flare by *Hinode*/Filtergram (FG) at 21:15 UT on October 24. Orange lines indicate contours of half-turn twist ($T_n = -0.5$) calculated from the NLFFF at 19:00 UT, which is approximately 2h before the X3.1-class flare. (b) NLFFF superimposed on (a) except without the twist contours. Field lines are selected both of whose footpoints are anchored on the enhanced region of Ca II; color shows the strength of the current density $|\mathbf{J}|$. (c) Strongly twisted lines with more than half-turn twist are added to the field lines shown in (b). Twisted lines start from region A (shown in (a)) and the other footpoint is anchored in region B (also shown in (a)). Strong enhancement of Ca II was not observed there during the flare. (d) Side view of (c).

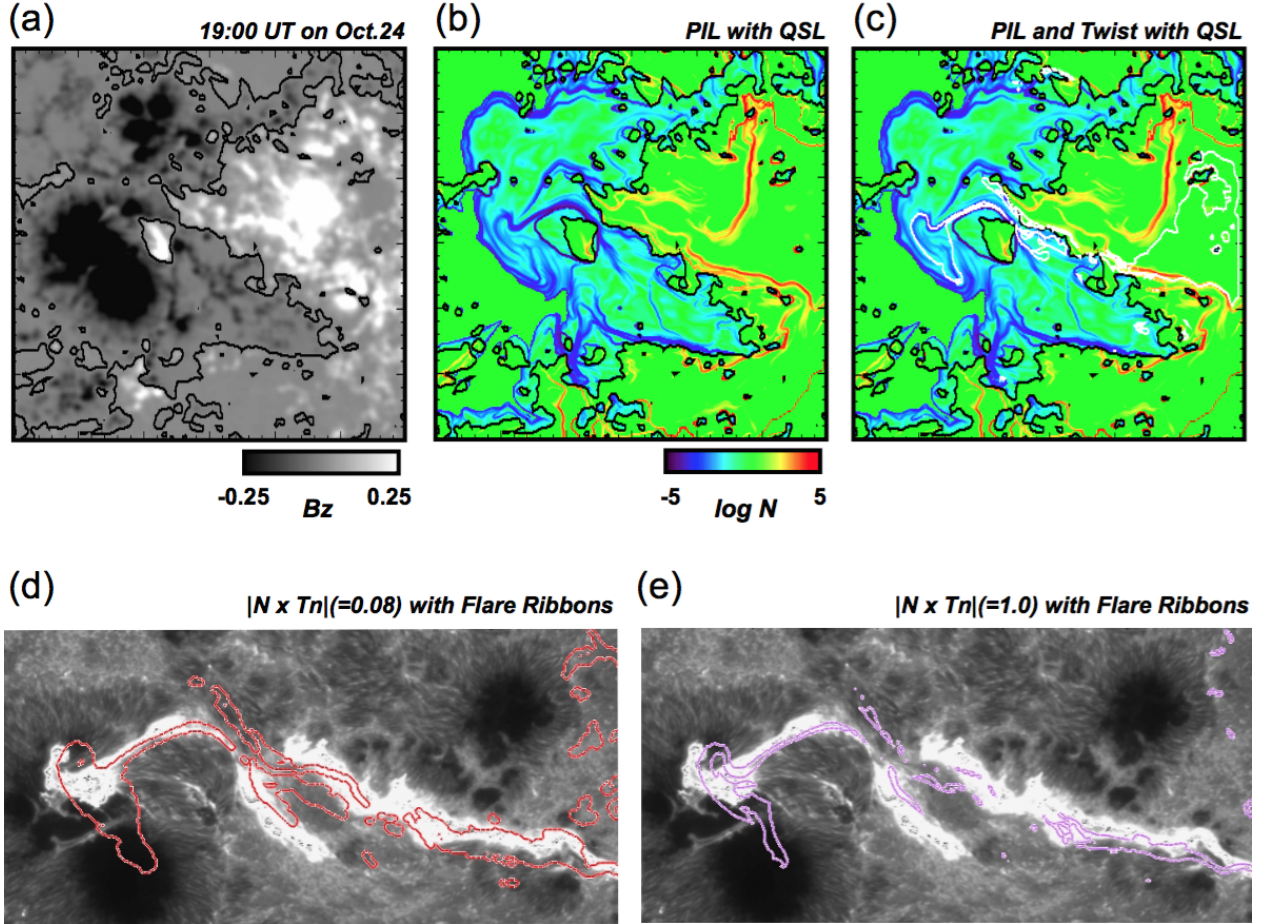


Fig. 6.— (a) B_z distribution with PIL before the flare observed at 19:00 UT on October 24. (b) Distribution of the norm $N(x, y)$ derived from the NLFFF extrapolated from the photospheric field in (a) together with the PIL, whose size corresponds to (a). (c) PIL and twist contour $T_n = -0.5$ obtained from the NLFFF plotted in black and white, respectively, with N distribution. (d) Correspond of $|T_n \times N| = 0.08$ (red lines) superimposed on flare ribbons observed at 21:15 UT by *Hinode*. The calculation of $|T_n \times N|$ is satisfied for both $T_n < -0.5$ and $|N| > 1$. (e) Same as (d) except that the contour level of $|T_n \times N|$ (purple) is 1.0.

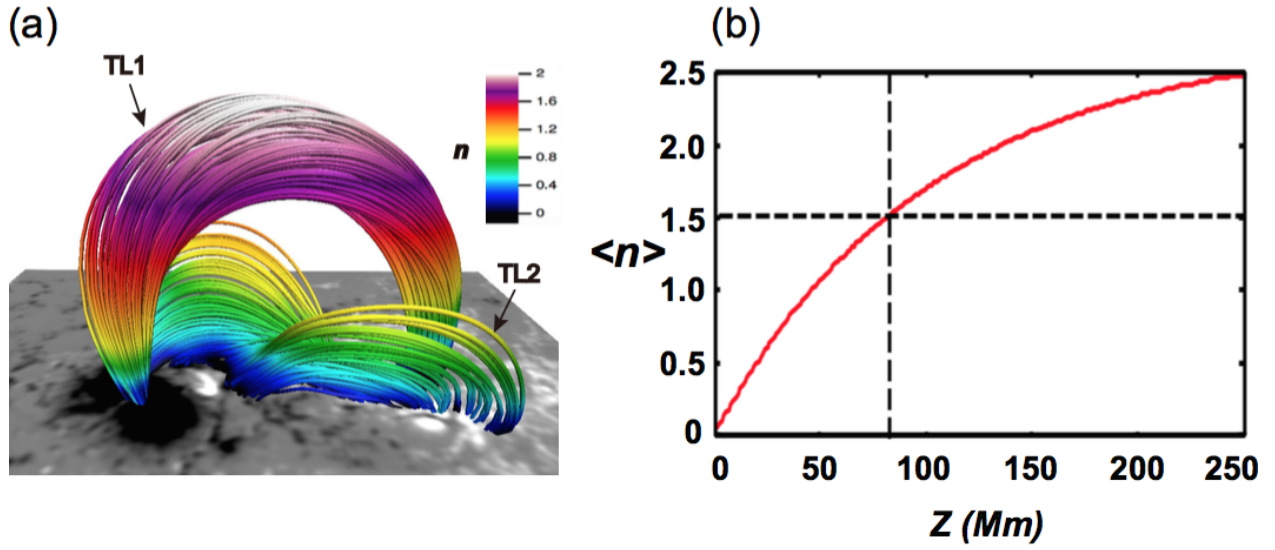


Fig. 7.— (a) Three-dimensional magnetic field lines of the NLFFF with more than half-turn twist are plotted. Color indicates the value of the decay index n , and the B_z distribution on the bottom surface, all of which are observed at 19:00 UT (before the flare). Each arrow indicates a flux tube reconstructed in the NLFFF. (b) Average decay index defined by Equation (10) in height profile, which is calculated in a range of $0.25L_0 \leq x \leq 0.75L_0$ and $0.2L_0 \leq y \leq 0.7L_0$ for $N_x=N_y=150$. Vertical and horizontal dashed lines cross at the threshold of the torus instability inferred from the theory.

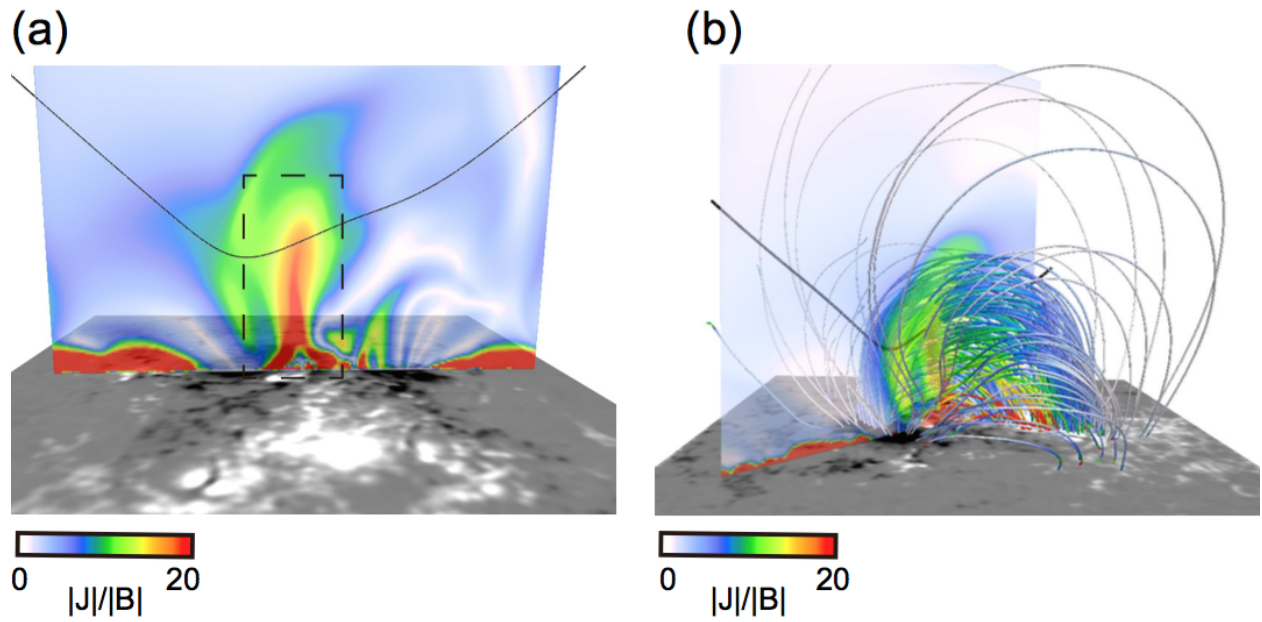


Fig. 8.— (a) $|\mathbf{J}|/|\mathbf{B}|$ drawn on a vertical cross section, that is a side view from the west side obtained from the NLFFF before the flare. Black solid line indicates contour of $n=1.5$, and vertically elongated current is surrounded by the dashed square. (b) Field lines colored according to $|\mathbf{J}|/|\mathbf{B}|$ superimposed on the B_z distribution. Format of the vertical cross section and solid line are identical to those in (a) except that the angle is different.

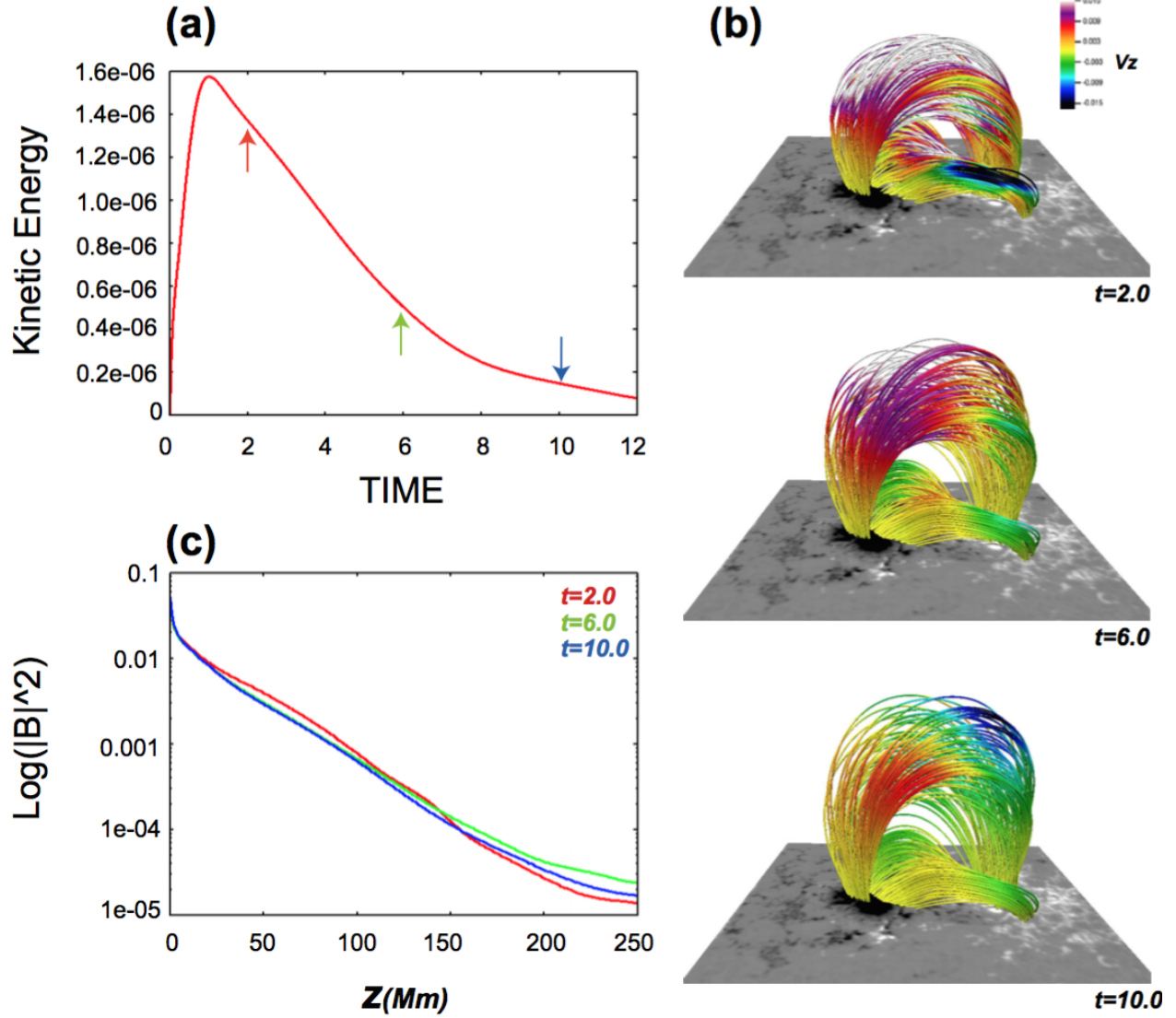


Fig. 9.— Results from the MHD simulation. (a) The temporal evolution of the kinetic energy, that is marked with each colored arrow at $t=2.0$, $t=6.0$, and $t=10.0$, respectively. (b) The temporal evolution of the 3D magnetic structures at each time marked with the colored arrows in (a) where the color on the field lines indicates a distribution of the vertical velocity. (c) Vertical profiles of $|\mathbf{B}|^2$ at center of the numerical box where the red, green and blue lines correspond to those at $t=2.0$, $t=6.0$, and $t=10.0$, respectively.